CHINESE OPTICS LETTERS

Vol. 22, No. 3 | March 2024

Talbot effect in anti-PT symmetric synthetic photonic lattices

Zhaofeng Liu (刘兆峰)[1], Siwei Tang (唐思维)[1], Zengrun Wen (温增润)[1*], Yuanmei Gao (高垣梅)[1], Yangjian Cai (蔡阳健)[1,2**], and Liren Zheng (郑立仁)[1***]

[1] Shandong Provincial Engineering and Technical Center of Light Manipulations & Shandong Provincial Key Laboratory of Optics and Photonic Device, School of Physics and Electronics, Shandong Normal University, Jinan 250358, China

[2] School of Physical Science and Technology, Soochow University, Suzhou 215006, China

*Corresponding author: wenzengrun@163.com

**Corresponding author: yangjiancai@sdnu.edu.cn

***Corresponding author: zlrgym@sdnu.edu.cn

Received September 26, 2023 | Accepted November 3, 2023 | Posted Online March 21, 2024

We investigated the Talbot effect in an anti-parity-time (PT) symmetric synthetic photonic lattice composed of two coupled fiber loops. We calculated the band structures and found that with an increase in the gain-loss parameter, the band transitions from a real spectrum to a complex spectrum. We study the influence of phase in the Hermitian operator on the Talbot effect, and the Talbot effect disappears when the period of the input field is $N > 8$. Further study shows that the variation of Talbot distance can also be modulated by non-Hermitian coefficients of gain and loss. This work may find significant applications in pulse repetition-rate multiplication, temporal invisibility, and tunable intensity amplifiers.

Keywords: Talbot effect; synthetic dimensions; anti-PT symmetry; photonic lattices.

DOI: 10.3788/COL202422.031901

1. Introduction

The Talbot effect, initially discovered by H. F. Talbot in 1836[1], refers to the self-replication phenomenon of periodic structures[2] under quasi-monochromatic coherent light illumination, which directly arises from near-field Fresnel diffraction[3]. The Talbot distance Z_T is defined as the position at which waves periodically reproduce themselves along the propagation direction[4]. In addition to optics, this effect has also been widely studied and applied in condensed matter[5,6], quantum revivals[7,8], X-ray[9,10], plasmonic[11,12], electron[13,14], prime-number decomposition[15], and so on. Currently, research on the optical Talbot effect has expanded from the spatial domain[16–18] to the temporal domain[19–21], from linear to nonlinear[22], and from continuous media to discrete systems[16–18,23]. Unlike in continuous media, the occurrence of the Talbot effect in discrete media requires the pattern period to meet specific conditions[4,18], whether in one-dimension[24] or two-dimensions[25].

The non-Hermitian Hamiltonians have completely real spectra if they obey parity-time (PT) symmetry, which was proved by Bender and their colleagues[26,27]. The anti-PT symmetry demands that the refractive index $n(x) = n_R(x) + in_I(x)$ should satisfy $n(-x) = -n^*(x)$[28,29]. This means that the real part $n_R(x)$, the phase distribution, should be an odd function, while the imaginary part $n_I(x)$, the gain/loss, should be an even function. PT-symmetry in optics was initially observed in the context of two coupled waveguides[30,31]. However, experimental achievement on an anti-PT symmetric large-scale lattice is highly limited. To overcome limitations, recently, there has been a generalization of the lattice concept from real space to synthetic dimensions, including temporal and spectral lattices[32,33]. By representing a temporal grid lattice, the evolution of pulses in two coupled fiber rings can be analogous to the dynamics of light beams in a spatial grid lattice[19]. Through temporal control of gain and loss within the lattice structure[34,35], researchers have, to the best of their knowledge, successfully achieved experimental realization of PT-symmetry in large-scale lattices for the first time[36].

In this study, we employ an anti-PT symmetric synthetic photonic lattice composed of two coupled fiber loops. Electro-optic and acousto-optic modulators are utilized to adjust the phase distribution as well as gain and loss coefficients of the system. First, the band structure is calculated, followed by a theoretical analysis of the conditions for generating the Talbot effect and the calculation method of the Talbot distance. Additionally, simulations are conducted under two scenarios, Hermitian phase modulation and non-Hermitian modulation, to investigate the Talbot self-imaging phenomenon. The goal is to explore the

influence of these different modulation methods on the Talbot effect and the characteristics of self-imaging.

2. Model and Theory

The anti-PT symmetric synthetic photonic lattice is formed by two coupled fiber loops, which are shown in Fig. 1(a). A 50:50 directional coupler connects two fiber rings with a length difference ΔL[19,29]. Once the coupler receives the initial light pulse injected into the long loop, it generates two new pulses that flow into each loop. After completing one round trip, the pulses in the short loop return to the coupler first, and subsequently propagate in the long loop. As a result, the two pulse trains interfere with each other through the coupler[20]. Like the dynamics of beams in spatial grids, the pulse train undergoes incremental evolution as the number of round trips increases. The equivalent lattice in the time domain is shown in Fig. 1(b), where m is the number of pulses entering the coupler, and n is the position of the pulse in the lattice.

As mentioned in the introduction section, to guarantee the odd symmetry of the real part, the phase modulator needs to be adjusted so that φ_n satisfies

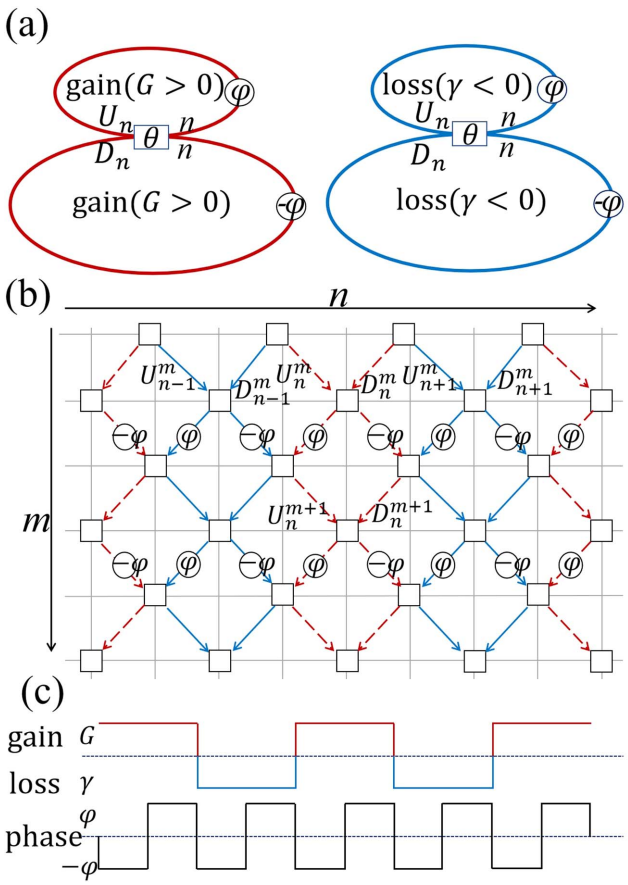

Fig. 1. Schematic of anti-PT symmetric synthetic photonic lattice. (a) Two coupling fiber loops with a length difference and (b) corresponding temporal mesh lattice with anti-PT symmetry. (c) Distribution of the phase, gain, and loss.

$$\varphi_n = \begin{cases} -\varphi, & n = 2k \\ +\varphi, & n = 2k+1 \end{cases}, \tag{1}$$

where φ is the amplitude of phase modulation, $k \in \mathbf{Z}$. The distributions of φ_n, gain, and loss are shown in Fig. 1(c).

Similarly, to ensure that the imaginary part is an even function, the acousto-optic modulator needs to be adjusted, and the gain ($G > 0$) and loss ($\gamma < 0$) are set as

$$\begin{cases} \gamma_p = \gamma, \gamma_q = G, & \text{for} \quad \mathrm{mod}(n+3;4) = 0 \\ \gamma_p = \gamma, \gamma_q = \gamma, & \text{for} \quad \mathrm{mod}(n+3;4) = 1 \\ \gamma_p = G, \gamma_q = \gamma, & \text{for} \quad \mathrm{mod}(n+3;4) = 2 \\ \gamma_p = G, \gamma_q = G. & \text{otherwise} \end{cases}. \tag{2}$$

Assuming that the amplitudes of the pulses in the short and long loops are U_n^m and D_n^m, respectively, the pulse iteration equation governing the dynamics in the anti-PT symmetric synthetic photonic lattice can be expressed as

$$\begin{cases} U_n^{m+1} = \frac{1}{\sqrt{2}} e^{\gamma_p} (U_{n+1}^m + i D_{n+1}^m) e^{-i\varphi_n} \\ D_n^{m+1} = \frac{1}{\sqrt{2}} e^{\gamma_q} (D_{n-1}^m + i U_{n-1}^m) \end{cases}. \tag{3}$$

To better study the optical pulse transmission characteristics in the synthesized photonic lattice, we use $e^{ikn}e^{i\beta m}$ to solve the dispersion relation of the system. The Bloch mode is $(U_n^m, D_n^m)^T = (U, D)^T e^{ikn} e^{i\beta m}$, where $(U, D)^T$ is the periodic Bloch function, k and β represent the transverse Bloch momentum and longitudinal propagation constant, respectively[36,37]. By inserting Eqs. (1) and (2) and the Bloch mode $(U_n^m, D_n^m)^T = (U, D)^T e^{ikn} e^{i\beta m}$ into Eq. (3), we can obtain the dispersion relation

$$\begin{aligned} \cos(4k) = {} & 2 + 4\cos(4\beta) + \cos(2\varphi) \\ & + 8\cos(2\beta)\cos\varphi\cosh(2G) + 2\cosh(4G). \end{aligned} \tag{4}$$

The band structure can be manipulated by adjusting the wave vector k, the phase φ, and the gain G (loss γ). For $G = 0$, Eq. (4) becomes $\cos(4k) = 4 + 4\cos(4\beta) + \cos(2\varphi) + 8\cos(2\beta)\cos(\varphi)$. The band structures with different values of φ have been investigated[29].

Next, as $\varphi = \pi/2$, the dispersion relationship is simplified as $\cos(4k) = 1 + 4\cos(4\beta) + 2\cosh(4G)$. Figure 2 illustrates the band structures with various gain G. In Fig. 2(a), the band structures become entirely real and exhibit anomalies. In Figs. 2(b)–2(e), the bands exhibit both real and imaginary parts. However, in Fig. 2(f), the bands become entirely imaginary.

Considering the essential prerequisites for the occurrence of the Talbot effect in the synthetic photonic lattice, we assume that the input field has the period N in the time domain grid. Due to transverse discreteness, N is an integer[19]. Therefore, the period of the incident pulse train in the coupling loop is $N\Delta T$. To satisfy the periodic boundary condition, the Bloch momentum is $k_l = 2\pi l/M$, where $M = N/4$ and $l = 0, 1, 2, \ldots, M-1$. The propagation constant corresponding to the Bloch momentum k_l is expressed as $\beta_{j,l}$, where j is the band index and is equal

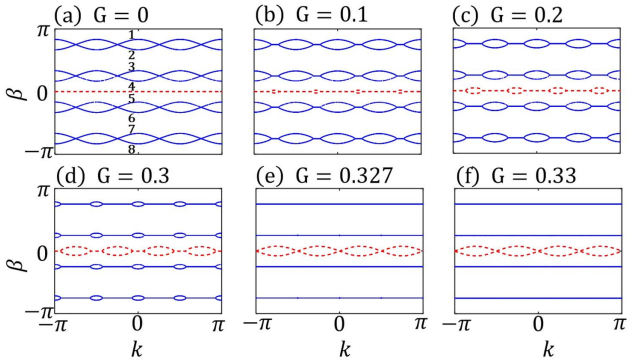

Fig. 2. Band structures for $G = 0$, $G = 0.1$, $G = 0.2$, $G = 0.3$, $G = 0.327$, and $G = 0.33$, respectively. $\varphi = \pi/2$. The blue line represents the real part of the band, and the red line represents the imaginary part of the band.

to 1, 2, 3, 4, 5, 6, 7, and 8. The propagation constant at the fourth band is $\beta_{4,l} = \frac{1}{4}\arccos(\frac{1}{4}(-1 + \cos(4k_l) - 2\cosh(4G)))$.

The Bloch superposition is used to describe the evolution of the field,

$$\begin{pmatrix} U_n^m \\ D_n^m \end{pmatrix} = \sum_{j=1}^{8}\sum_{l=0}^{M-1} c_{j,l}\begin{pmatrix} U_{j,l} \\ D_{j,l} \end{pmatrix}\exp(ik_l n)\exp(i\beta_{j,l}m). \quad (5)$$

Recovery can occur only when $\beta_{j,l}$ satisfies $\lambda_{j,l}\beta_{j,l}/2 = 2\mu_{j,l}\pi$, where $\lambda_{j,l}$ is the recovery distance, and $\mu_{j,l}$ is a nonzero integer. Since the time-domain grid is discrete in the propagation direction and $\lambda_{j,l}$ is an integer, $\beta_{j,l}$ should be a rational multiple of π[19]. Therefore, the Talbot distance is $Z_T = \mathrm{LCM}(\lambda_{1,0}, \lambda_{1,1}, \ldots, \lambda_{1,M}, \lambda_{2,0}, \ldots, \lambda_{8,M})$, where LCM is the least common multiple.

3. Results and Discussion

3.1. Talbot effect of Hermitian phase modulation

First, we study the influence of the phase of the Hermitian operator on the Talbot effect. For $N = 4$, the gain factor takes a value of $G = 0$. Considering the periodic boundary conditions with $k_0 = 0$, the propagation constant is $\beta_{4,0} = \frac{1}{2}\arccos(\frac{1}{2}(1-\cos\varphi))$, and the Talbot effect occurs when the mode of $\beta_{4,0}$ can be replicated during propagation. Assuming efficient recovery of the $\beta_{4,0}$ mode, we can express $\beta_{4,0}$ as $p\pi/q$, where p and q are relatively prime integers.

For odd p and q, the modal recovery distance for $\beta_{4,0}$ is $\lambda_{j,l} = 4q$. For $G = 0$, $\varphi = 0$, and $\beta_{4,0} = \pi/4$, according to the symmetry of the bands, the propagation constants are $\beta_{1,0} = 3\pi/4$, $\beta_{2,0} = \pi/2$, and $\beta_{3,0} = \pi/2$. The recovery distances are $\lambda_{1,0} = 16$, $\lambda_{2,0} = 8$, $\lambda_{3,0} = 8$, and $\lambda_{4,0} = 16$. Thus, the Talbot distance is $Z_T = 16$. In Fig. 3(a1), the evolution of the pulse intensity is the Talbot effect plot, where the pulse train achieves complete recovery every 16 steps. At $m = 8$, the intensity distribution is the same as the initial distribution at $m = 0$, which only accumulates a π phase delay. For $\varphi = \pi/2$, according to the symmetry of the bands, the corresponding propagation constants of the

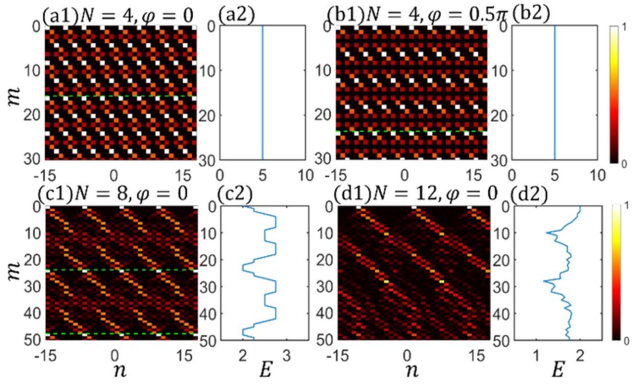

Fig. 3. (a1), (b1) The pulse intensity evolution in the long loop is shown for $\varphi = 0$ and $\varphi = 0.5\pi$, respectively. The input period is $N = 4$. (c1), (d1) The pulse intensity evolution in the long loop is shown for $N = 8$ and $N = 12$ with $\varphi = 0$. The green dotted line is the location of the Talbot images.

bands are $\beta_{1,0} = 5\pi/6$, $\beta_{2,0} = 2\pi/3$, $\beta_{3,0} = \pi/3$, and $\beta_{4,0} = \pi/6$. The recovery distances are $\lambda_{1,0} = 24$, $\lambda_{2,0} = 12$, $\lambda_{3,0} = 12$, and $\lambda_{4,0} = 24$. Thus, the Talbot distance is $Z_T = 24$. The corresponding Talbot diagram is presented in Fig. 3(b1). For $N = 8$ and $\varphi = \pi/2$, the Bloch momentums are $k_0 = 0$ and $k_1 = \pi$, and the propagation constants of the fourth band are

$$\beta_{4,0} = \frac{1}{4}\arccos\left(-\frac{1}{2}\cosh(4G)\right),$$
$$\beta_{4,1} = \frac{1}{4}\arccos\left(-\frac{1}{2}\cosh(4G)\right). \quad (6)$$

To support recovery, $\beta_{4,0}$ and $\beta_{4,1}$ are both in the form of $p\pi/q$. The Talbot effect occurs only when G equals zero, and the Talbot distance is $Z_T = 24$, as shown in Fig. 3(c1). Due to the periodic incidence conditions and transverse discreteness, the set of N should be restricted to $\{4, 8, 12, \ldots, 2M_L\}$, where M_L is the longest transmission distance. For $N > 8$, the Talbot effect does not occur. We use the case of $N = 12$ as an example for illustration. For $N = 12$, the corresponding Bloch momentum is $k_1 = 2\pi/3$, and the propagation constant is $\beta_{4,1} = \frac{1}{4}\arccos(-\frac{7}{8})$ and is no longer rational multiples of π. Consequently, the condition required for the Talbot effect, as illustrated in Fig. 3(d1), is not satisfied, the propagation image along the propagation direction does not exhibit periodic recovery, and the energy shows irregular oscillation.

On the other hand, the Talbot distance can be manipulated by applying linear phase modulation to the incident pulse train. We denote the interval between adjacent pulse phase shifts as φ_0. In Fig. 4, the input field of the temporal grid also has an initial momentum φ_0, which causes the Bloch momentum to become $k_l = 2\pi l/M + \varphi_0$. For $N = 4$, the fourth band with the corresponding transmission constant is $\beta_{4,0} = \frac{1}{4}\arccos(\frac{1}{4}(-1+\cos(4\varphi_0) - 2\cosh(4G)))$. The Talbot effect exists only when $\beta_{4,0}$ is a rational multiple of π, and we express $\beta_{4,0}$ as $a\pi/b$, where a and b are positive integers of relative prime numbers. Since $-\pi < \varphi_0 < \pi$ and $0 \le G < 0.33$, the range of values for $\beta_{4,0}$ is

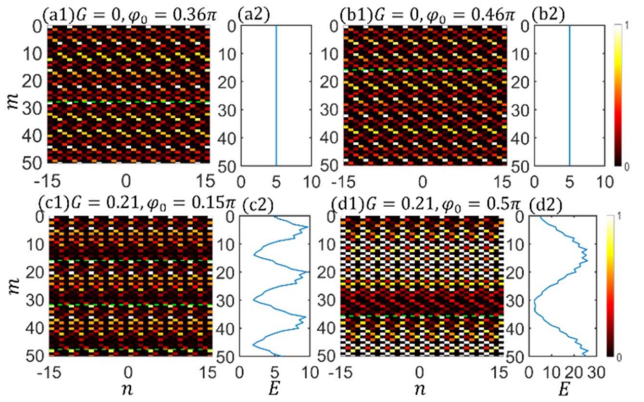

Fig. 4. Input pulse period $N=4$. (a1), (b1) Talbot carpets for $\varphi_0=0.36\pi$ and $\varphi_0=0.46\pi$. $G=0$. (c1), (d1) Talbot carpets for $\varphi_0=0.15\pi$ and $\varphi_0=0.5\pi$. $G=0.21$.

$(\pi/4, \pi/3]$. b should be at least 3, and the corresponding Talbot distance is $Z_T=12$. The set of Talbot distances is denoted by $\{12, 16, 20, \ldots, 4b, \ldots, M_L\}$. For $G=0$, when φ_0 takes the values of 0.36π and 0.46π, it corresponds to $Z_T=28$ and $Z_T=16$, respectively. For $G=0.21$, when φ_0 takes the values of 0.15π and 0.5π, it corresponds to $Z_T=28$ and $Z_T=36$, respectively. The corresponding Talbot images are depicted in Figs. 4(a1)–4(d1).

3.2. Non-Hermitian modulated Talbot effect

The Talbot effect can also be observed by modifying the non-Hermitian coefficients of gain and loss. For $N=4$ and $\varphi=0$, the fourth band propagation constant is $\beta_{4,0}=\arccos\sqrt{\frac{1}{2}-\frac{\cosh(G)^2}{4}-\frac{\sinh(G)^2}{4}+\frac{1}{4}\sqrt{1-4\cosh(G)^2\sinh(G)^2}}$. When the gain coefficients are $G=0.29$ and $G=0.35$, respectively, the propagation constants of the fourth band are $\beta_{4,0}=3\pi/8$ and $\beta_{4,0}=3\pi/10$. The corresponding Talbot distance is $Z_T=32$ and $Z_T=40$, and the Talbot images are shown in Figs. 5(a1) and 5(b1).

Then, we investigated the case where N equals 4 and φ equals π. We found that when the gain-loss coefficient and the input pulse period are identical, the Talbot effect and the amplitude of energy remain consistent for the two initial phases of $\varphi=0$ and $\varphi=\pi$.

For $N=4$ and $\varphi=\pi/2$, according to Fig. 2, the first and second bands are symmetrical with respect to $\beta=3\pi/4$, the third band is symmetrical with the fourth band $\beta=\pi/4$, and the first (second) band is symmetrical with the fourth (third) band about $\beta=\pi/2$. The fourth band propagation coefficient is $\beta_{4,0}=\frac{1}{4}\arccos(-\frac{1}{2}\cosh(4G))$. The Talbot effect occurs when $\beta_{4,0}$ is a rational multiple of π, expressed as $p\pi/q$. In this case, the Talbot distance can be calculated as $4q$. Considering that the gain-loss factor falls within the range of $0\le G<0.33$, the propagation constant $\beta_{4,0}$ is in the range of $\pi/8$ to $\pi/4$, with q being at least 5. Thus, the Talbot distance falls within the range $\{20, 24, 28, \ldots, 4q, \ldots, M_L\}$. Accompanying the energy oscillations during Talbot imaging, for $G=0.25$, the propagation constant of the fourth band is $\beta_{4,0}=\pi/5$. Consequently, the corresponding Talbot distance is $Z_T=20$, which is illustrated in Fig. 5(c1). For $G=0.31$, the propagation constant of the fourth band is $\beta_{4,0}=2\pi/9$, corresponding to the Talbot distance $Z_T=36$, as shown in Fig. 5(d1). From Figs. 5(c1) and 5(d1), the amplitude of energy oscillation increases as the gain-loss factor augments. For $G\ge0.33$, the band structure becomes entirely imaginary; as illustrated in Fig. 2(f), the input field distribution cannot be recovered due to varying degrees of amplification or attenuation experienced by these modes. Therefore, when the included modes are excited in the purely imaginary region of the band structure, the Talbot effect does not occur. We attempted to utilize the enumeration method to detect the presence of the Talbot effect for $N>4$. However, the Talbot effect does not occur.

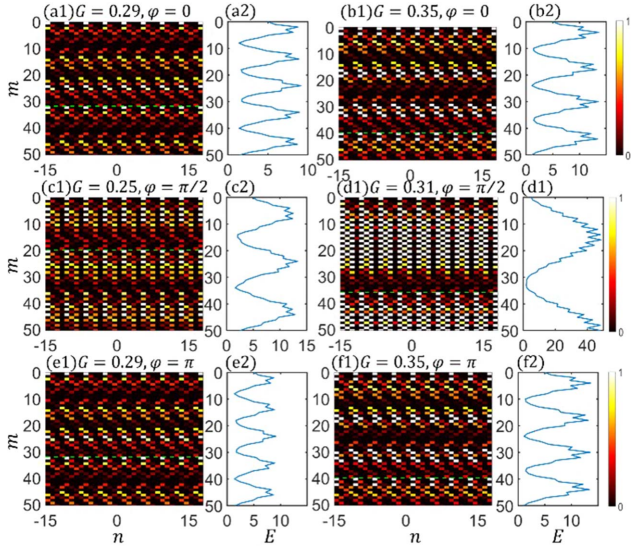

Fig. 5. (a1), (b1) Talbot carpets for $G=0.29$ and $G=0.35$. $\varphi=0$. (c1), (d1) Talbot carpets for $G=0.25$ and $G=0.31$. $\varphi=\pi/2$. (e1), (f1) Talbot carpets for $G=0.29$ and $G=0.35$. $\varphi=\pi$.

The influence of parameters φ and γ on the energy bands is depicted in Fig. 6. When above the curve, all eigenvalues of the

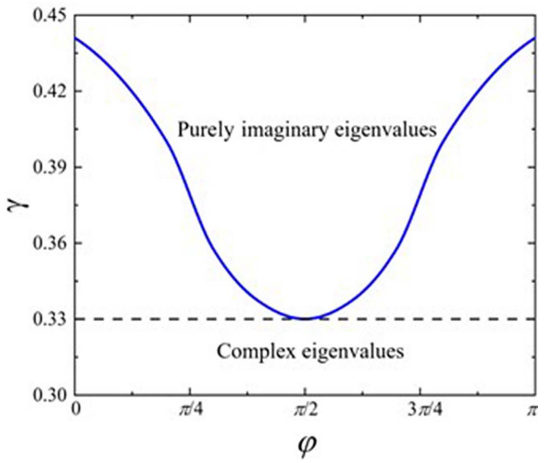

Fig. 6. The curve representing the anti-PT symmetry breaking threshold in a two-dimensional parameter space of φ and γ.

system are completely imaginary. When on the curve, symmetry breaking occurs. Below the line, the eigenvalues of the system are complex, representing a complex spectrum with both real and imaginary components. It is evident that the curve exhibits symmetry with respect to the $\varphi = \pi/2$ axis.

4. Conclusion

In summary, we constructed an anti-PT symmetric synthetic photonic lattice using two coupled fiber loops. We presented the corresponding equivalent lattice diagram and derived the pulse amplitude expression for light pulses in the double loops. Then, we obtained the dispersion relation of the system using discrete plane wave solutions and plotted the band structure by varying phase values and gain-loss coefficients. Furthermore, we analyzed and studied the Talbot effect in the anti-PT symmetric synthetic photonic lattice under both Hermitian and non-Hermitian phase modulation. The research revealed that when the input period is $N = 2, 4, 6, 8$, the Talbot distance can be flexibly controlled by changing the gain and loss factors or linearly modulating the input pulse sequence. Additionally, at $\varphi = \pi/2$, when the gain-loss factor is greater than or equal to 0.33, the Talbot effect disappears. If the pulse input period, gain, and loss coefficients are the same, the band structures corresponding to the pulse phases $\varphi = 0$ and $\varphi = \pi$ exhibit the same patterns, resulting in the same Talbot effect and associated energy oscillations. This work may find promising applications in pulse repetition-rate multiplication, temporal cloaking, and tunable intensity amplifiers.

Acknowledgements

This work was supported by the National Key Research and Development Program of China (Nos. 2022YFA1404800 and 2019YFA0705000), the National Natural Science Foundation of China (Nos. 12104272, 12274270, 91950104, 12192254, 92250304, and 11974218), and the Local Science and Technology Development Project of the Central Government (No. YDZX20203700001766).

References

1. H. F. Talbot, "LXXVI. Facts relating to optical science. No. IV," Philos. Mag. **9**, 401 (2009).
2. L. A. Hall, S. Ponomarenko, and A. F. Abouraddy, "Temporal Talbot effect in free space," Opt. Lett. **46**, 3107 (2021).
3. J. T. Winthrop and C. R. Worthington, "Theory of Fresnel images. I. Plane periodic objects in monochromatic light," J. Opt. Soc. Am. A. **55**, 373 (1965).
4. K. Zhan, X. Kang, Q. Zhang, *et al.*, "Discrete Talbot effect in reciprocal and nonreciprocal dimer lattices," J. Opt. Soc. Am. B. **39**, 3283 (2022).
5. V. Makhalov and A. Turlapov, "Order in the interference of a long chain of Bose condensates with unrestricted phases," Phys. Rev. Lett. **122**, 090403 (2019).
6. J. Feng, Z. Zhang, and M. Xiao, "Talbot effects induced by gain-loss modulated optical lattices in a coherent atomic medium," Phys. Rev. A. **103**, 063516 (2021).
7. F. Chamizo and O. P. Santillán, "About the quantum Talbot effect on the sphere," J. Phys. A **56**, 255302 (2023).
8. P. Mantashyan, G. Mantashian, and D. Hayrapetyan, "Talbot effect in InAs/GaAs coupled cylindrical quantum dots ensemble," Phys. E **148**, 115662 (2023).
9. M. Balyan, L. Levonyan, and K. Trouni, "X-ray dynamical diffraction Talbot effect behind a crystal in free space," Acta. Cryst. A **77**, 149 (2021).
10. M. K. Balyan, "X-ray dynamical diffraction analogues of the integer and fractional Talbot effects," J. Synchrotron Rad. **26**, 1650 (2019).
11. H. Ma, S. Su, H. Zhou, *et al.*, "Tunable plasmonic talbot effect based on graphene monolayer," Appl. Sci. **10**, 4782 (2020).
12. S. Farhadi, A. Farmani, and A. Hamidi, "Figure of merit enhancement of surface plasmon resonance biosensor based on Talbot effect," Opt. Quantum Electron. **53**, 518 (2021).
13. M. V. Tsarev, A. Ryabov, and P. Baum, "Free-electron qubits and maximum-contrast attosecond pulses via temporal Talbot revivals," Phys. Rev. Res. **3**, 043033 (2021).
14. G. Calogero, N. R. Papior, B. Kretz, *et al.*, "Electron transport in nanoporous graphene: probing the Talbot effect," Nano. Lett. **19**, 576 (2019).
15. K. Pelka, J. Graf, T. Mehringer, *et al.*, "Prime number decomposition using the Talbot effect," Opt. Express **26**, 15009 (2018).
16. K. Li, F. Xia, M. Wang, *et al.*, "Discrete Talbot effect in dielectric graphene plasmonic waveguide arrays," Carbon **118**, 192 (2017).
17. K. Zhan, L. Dou, R. Jiao, *et al.*, "Talbot effect in arrays of helical waveguides," Opt. Lett. **46**, 322 (2021).
18. X. Kang, H. Wang, L. Dou, *et al.*, "Discrete Talbot effect in modulated lattices with PT symmetric perturbations," J. Opt. Soc. Am. B. **40**, 856 (2023).
19. S. Wang, B. Wang, and P. Lu, "PT-symmetric Talbot effect in a temporal mesh lattice," Phys. Rev. A. **98**, 043832 (2018).
20. S. Wang, C. Qin, B. Wang, *et al.*, "Discrete temporal Talbot effect in synthetic mesh lattices," Opt. Express **26**, 19235 (2018).
21. Z. Wen, B. Lu, K. Wang, *et al.*, "Discrete optical propagation in one-dimensional synthetic mesh lattice," J. Opt. Soc. Am. B **37**, 3152 (2020).
22. L. Li, H. Liu, and X. Chen, "Dynamic manipulation of nonlinear Talbot effect with structured light," Opt. Lett. **46**, 1281 (2021).
23. K. Zhan, L. Dou, X. Kang, *et al.*, "Controllable discrete Talbot self-imaging effect in Hermitian and non-Hermitian Floquet superlattices," Opt. Express **30**, 35256 (2022).
24. R. Iwanow, D. A. May-Arrioja, D. N. Christodoulides, *et al.*, "Discrete Talbot effect in waveguide arrays," Phys. Rev. Lett. **95**, 053902 (2005).
25. Z. Chen, Y. Zhang, and M. Xiao, "Discrete Talbot effect in two-dimensional waveguide arrays," Opt. Express **23**, 14724 (2015).
26. C. M. Bender and S. Boettcher, "Real spectra in non-Hermitian Hamiltonians having PT symmetry," Phys. Rev. Lett. **80**, 5243 (1998).
27. D. C. Brody, C. M. Bender, and H. F. Jones, "Complex extension of quantum mechanics," Phys. Rev. Lett. **89**, 270401 (2002).
28. L. Ge and H. E. Türeci, "Antisymmetric PT-photonic structures with balanced positive- and negative-index materials," Phys. Rev. A. **88**, 053810 (2013).
29. Y. Yue, J. Li, Z. Zhang, *et al.*, "Interaction between double solitons in anti-PT symmetric synthetic photonic lattices," Opt. Commun. **529**, 129082 (2023).
30. A. Guo, G. J. Salamo, D. Duchesne, *et al.*, "Observation of PT-symmetry breaking in complex optical potentials," Phys. Rev. Lett. **103**, 093902 (2009).
31. C. E. Rüter, K. G. Makris, R. El-Ganainy, *et al.*, "Observation of parity–time symmetry in optics," Nat. Phys. **6**, 192 (2010).
32. S.-L. Wang, B. Wang, C.-Z. Qin, *et al.*, "Rabi oscillations of optical modes in a waveguide with dynamic modulation," Opt. Quantum Electron. **49**, 389 (2017).
33. I. D. Vatnik, A. Tikan, G. Onishchukov, *et al.*, "Anderson localization in synthetic photonic lattices," Sci. Rep. **7**, 4301 (2017).
34. R. El-Ganainy, K. G. Makris, D. N. Christodoulides, *et al.*, "Theory of coupled optical PT-symmetric structures," Opt. Lett. **32**, 2632 (2007).
35. Z. H. Musslimani, K. G. Makris, R. El-Ganainy, *et al.*, "Optical solitons in PT periodic potentials," Phys. Rev. Lett. **100**, 030402 (2008).
36. A. Regensburger, C. Bersch, M. A. Miri, *et al.*, "Parity-time synthetic photonic lattices," Nature **488**, 167 (2012).
37. M. Mohammad-Ali, A. Regensburger, U. Peschel, *et al.*, "Optical mesh lattices with PT symmetry," Phys. Rev. A **86**, 023807 (2012).